Nano Research

Open Access

Research Article

A dual-confined strategy growing 2D nonlayered $FeCr_2Te_4$ with coexisting ferrimagnetic-antiferromagnetic state

Zeting Zeng[1,§], Wei Zhao[1,§], Qitao Jiang[1,§], Yan Han[1], Rongkai Jiao[1], Zheng Zhang[1], Can Zhao[1], Wenjuan Ci[1,2], Wuhong Xue[1,2] ✉, Huisheng Zhang[1,2], and Xiaohong Xu[1,2] ✉

[1] *Key Laboratory of Magnetic Molecules and Magnetic Information Materials of Ministry of Education & School of Materials Science and Engineering, Shanxi Normal University, Taiyuan 030031, China*

[2] *Research Institute of Materials Science, Shanxi Key Laboratory of Advanced Magnetic Materials and Devices, Shanxi Normal University, Taiyuan 030031, China*

[§] *Zeting Zeng, Wei Zhao, and Qitao Jiang contributed equally to this work.*

Cite this article: *Nano Research*, **2026**, *19*, 94908675. https://doi.org/10.26599/NR.2026.94908675

ABSTRACT: The emergence of intrinsic two-dimensional (2D) magnetic materials has spurred exploration of exotic physical phenomena at the atomic limit, while also opening new avenues for the design of compact, ultra-low-power spintronic devices. In contrast to the widely studied layered magnets, the ternary nonlayered magnets with excellent stability remain relatively unexplored. A key challenge lies in the scalable fabrication of high-quality, large-area samples. Herein, we propose a dual-confined chemical vapor deposition strategy for the first-time synthesis of 2D nonlayered ferrimagnetic $FeCr_2Te_4$ nanosheets. The as-grown nanosheets exhibit lateral dimensions up to 400 μm and outstanding stability under high-temperature and harsh chemical conditions. The Curie temperature of the samples is independent of thickness. Notably, a temperature-tunable antiferromagnetic state emerges in thicker nanosheets, driven by weak interlayer exchange coupling. Furthermore, the nanosheets exhibit an extrinsic skew-scattering-dominated anomalous Hall effect, with a high carrier concentration of 10^{20} cm^{-3} and mobility exceeding 30 $cm^2 \cdot V^{-1} \cdot s^{-1}$. This work opens up new avenues for the synthesis of ternary nonlayered 2D magnetic materials and significantly expands the material platform for developing high-performance spintronic devices.

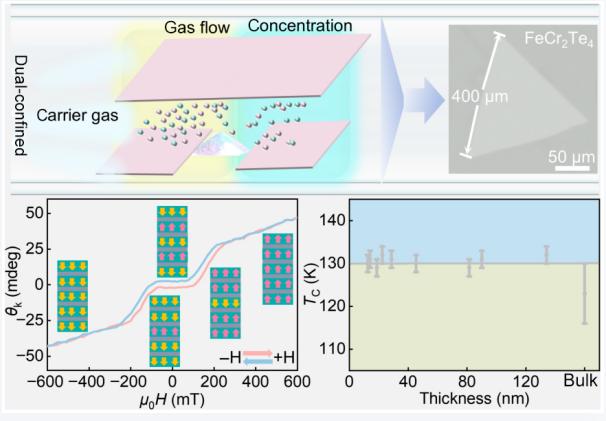

KEYWORDS: two-dimensional magnets, chemical vapor deposition, nonlayered materials, $FeCr_2Te_4$ nanosheets, ferrimagnetism, antiferromagnetic

1 Introduction

Intrinsic two-dimensional (2D) magnetic materials have fueled investigations into exotic physical phenomena at the atomic scale, while opening up new avenues for the development of compact, ultra-low-power spintronic devices [1, 2]. As an emerging frontier, these materials not only exhibit a diverse range of intriguing physical properties but also enable precise control over magnetism at the atomic level through external stimuli [3–8]. 2D magnetic materials are broadly categorized into layered and nonlayered magnetic systems [9]. To date, layered magnetic materials—including Fe_3GaTe_2 [3, 10], Fe_nGeTe_2 (n = 3, 4, 5) [11, 12], $Cr_2Ge_3Te_6$ [13], and CrI_3 [14]—constitute only a small subset of known crystalline structures. They typically suffer from poor environmental stability, complex synthesis routes, and limited crystal sizes, posing significant challenges for large-scale sample fabrication. In contrast, nonlayered 2D magnetic materials represent the majority of known crystalline structures. Among them, Fe-based and Cr-based compounds have attracted tremendous attention in low-dimensional magnetism research due to their compositional diversity, rich magnetic properties, and robust chemical stability. These materials also serve as pivotal candidates driving the advancement of spintronics and next-

Received: January 15, 2026; **Revised:** March 24, 2026
Accepted: March 25, 2026

✉Address correspondence to Wuhong Xue, xuewuhong@sxnu.edu.cn; Xiaohong Xu, xuxh@sxnu.edu.cn

generation information technologies. Within the family of Fe-based chalcogenides, several systems have been extensively investigated, including collinear antiferromagnetic (AFM) FeS [15], ferromagnetic (FM) $Fe_{5-7}Se_8$ [16, 17], and FeTe [18, 19]. Cr-based magnetic chalcogenides include ferrimagnetic (FIM) semiconducting Cr_2S_3 [20], AFM semi-metallic Cr_2Se_3 [21], and FM metallic Cr_5Te_8 [22, 23]. Despite these advances, current research on nonlayered 2D magnetic materials primarily focuses on binary systems, whereas their ternary and multinary counterparts remain in the early exploration stage.

Ternary compounds with the general formula AB_xX_y (where A and B represent transition metals, and X = S, Se, Te) exhibit distinct magnetic and electronic properties, such as metallic $CuCr_2Te_4$ [24], semi-metallic $HgCr_2Se_4$ [25], insulating $ZnCr_2S_4$ [26], and semiconducting $CrGeTe_3$ [27]. The diverse magnetic properties of the ternary $FeCr_2X_4$ family have garnered considerable research interest. For instance, cubic $FeCr_2S_4$ is a thickness-independent p-type FM semiconductor with a Curie temperature (T_C) of 170 K and exhibits a giant magnetoresistance (GMR) effect, whereas monoclinic $FeCr_2S_4$ is a thickness-independent AFM semiconductor with a Néel temperature (T_N) of 240 K [28, 29]. $FeCr_2Se_4$ is an AFM insulator with a T_N of 218 K, which undergoes a transition to a weak FM state below 75 K [30, 31]. Monoclinic $FeCr_2Te_4$ exhibits FIM behavior with a T_C of 120 K, accompanied by an observable anomalous Hall effect (AHE) [32–34]. To date, research on ternary $FeCr_2X_4$ compounds has primarily focused on bulk single crystals, with 2D $FeCr_2S_4$ nanosheets being the only ones successfully synthesized via chemical vapor deposition (CVD). It is well established that dimensional reduction in 2D materials can give rise to numerous unique physical properties. However, the low reactivity of Se and Te, which hinders the formation of stable chemical bonds with transition metals, poses a significant challenge for the synthesis of atomically thin $FeCr_2X_4$ (X = Se, Te) nanosheets [35]. Therefore, the successful fabrication of 2D $FeCr_2Te_4$ not only provides a novel route for the synthesis of multivalent tellurides and expands the library of 2D magnetic materials, but also advances our understanding of the interplay between dimensional reduction and magnetic behavior in nonlayered ternary systems.

In this work, we report the first synthesis of 2D $FeCr_2Te_4$ nanosheets on mica substrates using a dual-confined CVD strategy. The as-grown nanosheets achieve lateral dimensions of up to 400 μm with a uniform thickness distribution. Atomic structure characterization confirms the high crystalline quality of the as-prepared $FeCr_2Te_4$ nanosheets. These nanosheets exhibit out-of-plane (OP) FIM ordering, with magnetism originating from the competition between FM exchange interactions along Cr^{3+}–Te^{2-}–Cr^{3+} bonds and AFM interactions between Cr^{3+}–Fe^{2+} pairs. Polar magneto-optical Kerr effect (MOKE) measurements verify FIM ordering with a T_C of approximately 130 K, which remains independent of sample thickness. Notably, an emergent AFM state is observed in thicker $FeCr_2Te_4$ nanosheets. The formation of this AFM state is attributed to weak interlayer exchange coupling induced by variations in the van der Waals (vdW) interlayer spacing, and reversible switching between FIM and AFM states can be achieved through temperature modulation. In addition, transport measurements reveal that $FeCr_2Te_4$ nanosheets exhibit an AHE dominated by an extrinsic skew-scattering mechanism. This study not only provides critical insights into the growth of ternary nonlayered tellurides but also advances the fundamental understanding of magnetism in 2D nonlayered systems.

2 Experimental

2.1 CVD synthesis of $FeCr_2Te_4$ nanosheets

$FeCr_2Te_4$ nanosheets were grown on freshly cleaved mica substrates using a dual-confined CVD strategy. The dual confinement refers to the controlled restriction of both gas flow and precursor concentration during growth. A 2-inch tube furnace (KLG-12) equipped with a single independently controlled temperature zone was employed for the synthesis. A precursor mixture comprising $CrCl_3$ (Alfa Aesar, 99.9%), $FeCl_2$ (Alfa Aesar, 99.5%), and KCl (Alfa Aesar, 99.997%) in a weight ratio of 9:3:1 was placed at the center of the furnace. Te powder (200 mesh, 99%, Alfa) was positioned upstream in the same temperature zone, maintained at 500 °C. Prior to heating, the quartz tube was purged with 500 sccm of high-purity Ar for 20 min to eliminate residual oxygen and moisture. Subsequently, a carrier gas mixture of 150 sccm Ar and 10 sccm H_2 was introduced for sample growth at various heating temperatures, with each target temperature held constant for 10 min. Upon completion of growth, the furnace was slowly cooled to 400 °C, during which the H_2 flow was terminated and the Ar flow rate was adjusted to 200 sccm. The furnace was then fully opened and rapidly cooled to room temperature.

2.2 Sample transfer

Poly(methyl methacrylate) (PMMA) was employed as a transfer medium to facilitate subsequent characterization and measurements, enabling the transfer of $FeCr_2Te_4$ nanosheets grown on mica substrates onto both SiO_2/Si substrates and Cu grids. First, the PMMA solution was spin-coated onto the $FeCr_2Te_4$/mica samples at 2000 rpm. The samples were then heated at 150 °C for 7 min. This spin-coating and heating procedure was repeated twice. The PMMA-coated samples were immersed in deionized (DI) water for several minutes, after which the film was gently peeled off using tweezers and transferred onto the target substrates (SiO_2/Si or Cu grids). Finally, the PMMA layer was removed by immersion in acetone, followed by sequential rinsing with ethanol and DI water to eliminate residual polymer.

2.3 Device fabrication

$FeCr_2Te_4$ nanosheets were transferred onto SiO_2/Si substrates for device fabrication. Standard photolithography was performed using a direct laser writing system (MicroWriter Baby Plus, Durham Magneto Optical Ltd.) to define Hall bar electrode patterns. Subsequently, a Cr (~ 5 nm)/Au (~ 50 nm) bilayer was deposited by thermal evaporation, followed by lift-off in acetone to remove excess metal and complete the electrode patterning.

2.4 Sample characterizations

The morphology and thickness of the as-grown $FeCr_2Te_4$ nanosheets were characterized using optical microscopy (OM, CX40M, JinXiang) and atomic force microscopy (Bruker, Dimension Icon). Raman spectra were recorded with a Raman spectrometer (Horiba LabRAM HR Evolution) using a 532 nm excitation wavelength. The crystal structure was characterized by X-ray diffraction (XRD, Rigaku Ultima IV-185), and the chemical valence states were analyzed by X-ray photoelectron spectroscopy (XPS, ThermoFisher Scientific). Elemental composition and mapping were investigated using a thermal field emission scanning electron microscope (SEM, JEOL JSM-IT800) equipped with an energy-dispersive X-ray spectroscopy (EDS) detector. Atomic-scale

structure analysis was performed via annular dark-field scanning transmission electron microscopy (ADF-STEM, FEI Tecnai G2 F30). Temperature-dependent magnetotransport properties were measured using a Physical Property Measurement System (PPMS, Design Quantum Design DynaCool). Magnetic characteristics were further probed by magneto-optical Kerr effect (MOKE, Truth Instruments) and a magnetic property measurement system (MPMS, Quantum Design).

3 Results and discussion

Intrinsic submillimeter-scale 2D $FeCr_2Te_4$ nanosheets were successfully synthesized via a dual-confined CVD method in a single-zone tube furnace. The nonlayered $FeCr_2Te_4$ crystal adopts a monoclinic structure (space group: $I2/m$) with lattice parameters a = 6.822(2) Å, b = 3.938(1) Å, and c = 11.983(5) Å [32]. Each Fe and Cr atom coordinates with six Te atoms in an octahedral configuration, forming a 2R-stacking structure composed of alternating Fe and $CrTe_2$ layers. Figure 1(a) presents a schematic of the CVD synthesis process, along with an OM image and the corresponding crystal structure of the as-grown sample on a mica substrate. Freshly cleaved mica was employed as the growth substrate, with mica pieces of varying sizes placed at different positions in the precursor source zone. The dual-confined strategy enables the *in-situ* formation of a microreactor in the growth region, which not only modulates the gas flow rate to promote thinning of the nanosheets but also suppresses excessive nucleation, thereby facilitating the preferential formation of the ternary $FeCr_2Te_4$ phase. Consequently, the growth mechanism transitions from a thermodynamically controlled to a kinetically dominated regime [36]. During the growth process, a powder mixture of $FeCl_2$ and $CrCl_3$ served as the metal precursor, with KCl added as a fluxing agent. The addition of salts lowers the melting point of the precursors, promotes the formation of $CrCl_3$ intermediates, and suppresses the generation of binary impurity phases (Figs. S1(a) and S1(b) in the Electronic Supplementary Material (ESM)) [37]. The

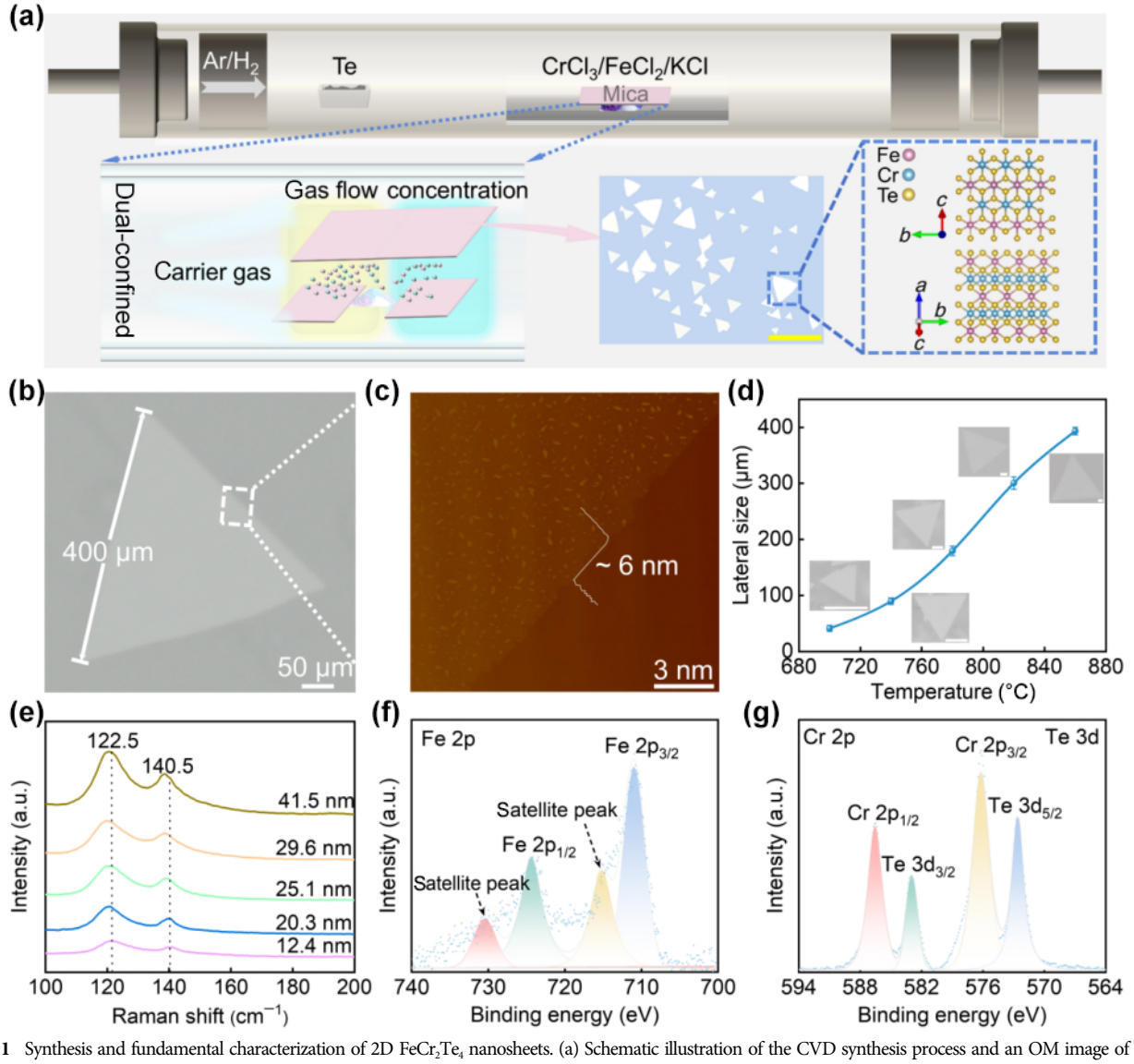

Figure 1 Synthesis and fundamental characterization of 2D $FeCr_2Te_4$ nanosheets. (a) Schematic illustration of the CVD synthesis process and an OM image of the as-grown samples on mica substrates. Scale bar: 50 μm. (b) and (c) OM and atomic force microscopy images of the largest nanosheets. (d) Temperature-dependent lateral sizes of the samples. Scale bar: 50 μm. (e) Thickness-dependent Raman spectra of the samples. (f) and (g) XPS spectra of Fe, Cr, and Te elements in the $FeCr_2Te_4$ nanosheets.

introduction of H_2 further facilitates the formation of highly reductive H_2Te. Collectively, these experimental results demonstrate that the salt-assisted dual-confined strategy enables the controlled synthesis of ultra-thin, large-area nonlayered $FeCr_2Te_4$ nanosheets.

The growth of $FeCr_2Te_4$ crystals is highly sensitive to the growth temperature. Figure 1(d) plots the lateral sizes of $FeCr_2Te_4$ nanosheets as a function of growth temperature. Corresponding atomic force microscopy and OM images of 2D $FeCr_2Te_4$ synthesized at different temperatures are provided in Figs. S2 and S3 in the ESM. At 860 °C, the synthesized 2D $FeCr_2Te_4$ nanosheets achieved a maximum lateral size of ~ 400 μm (Fig. 1(b)), with a thickness of ~ 6 nm (Fig. 1(c)). The observed surface roughness can be attributed to island-like features formed via secondary nucleation (Fig. S6 in the ESM). Figures S1(c) and S1(d) in the ESM show digital photographs of the large-area $FeCr_2Te_4$ nanosheets grown on the mica substrates. In addition to temperature, growth time and H_2 flow rate also modulate the lateral dimensions of $FeCr_2Te_4$ nanosheets (Figs. S4 and S5 in the ESM). Raman spectroscopy and XPS were employed to investigate the phonon modes and elemental composition of the $FeCr_2Te_4$ nanosheets. As shown in Fig. 1(e), the Raman spectra of nanosheets with varying thicknesses exhibit two distinct characteristic peaks at 122.5 and 140.5 cm^{-1}, corresponding to the OP A_{1g} mode and in-plane (IP) E_g mode of 2D tellurides, respectively. The Raman scattering intensity gradually decreases with decreasing nanosheet thickness. Concurrently, both the A_{1g} and E_g modes undergo a red shift as the thickness increases, which is primarily ascribed to variations in the covalent bonding strength among Cr, Fe, and Te atoms. This behavior is consistent with previously reported results for CVD-synthesized Cr_xTe_y nanosheets [38]. XPS characterization confirms the presence of Fe, Cr, and Te elements in the as-synthesized 2D $FeCr_2Te_4$ nanosheets. The Fe 2p, Cr 2p, and Te 3d spectra verify the valence states of Fe^{2+}, Cr^{3+}, and Te^{2-}, respectively, with a stoichiometric ratio close to 1:2:4 (Figs. 1(f) and 1(g)) [18, 38]. No peaks corresponding to oxidized species were detected, confirming the high crystallinity, phase purity, and chemical stability of the synthesized samples.

The crystal microstructure and quality of the $FeCr_2Te_4$ nanosheets were further corroborated by ADF-STEM. Typical ADF-STEM images confirm the presence of a hexagonal close-packed structure. The absence of detectable defects or twin boundaries indicates that the nanosheets possess high crystallinity (Fig. 2(a)). By comparing with the reported crystal structure of monoclinic $FeCr_2Te_4$, we confirm that the as-synthesized 2D $FeCr_2Te_4$ nanosheets are oriented along the (001) crystal plane. Figure 2(b) presents an enlarged ADF-STEM image of the blue-marked region in Fig. 2(a), which is consistent with the simulated atomic model of the $FeCr_2Te_4$ crystal. The interplanar spacings of the (002) and (220) lattice planes are calculated to be 3.87 and 2.56 Å, respectively. Notably, the ADF-STEM image exhibits nearly identical Z-contrast distribution to that of the simulated $FeCr_2Te_4$ image along the (001) plane (Fig. S7 in the ESM). The fast Fourier transform (FFT) diffraction pattern displays a set of diffraction spots with hexagonal symmetry, which matches the diffraction characteristics of $FeCr_2Te_4$ along the [001] zone axis (Fig. 2(c)). Figure 2(d) shows the intensity

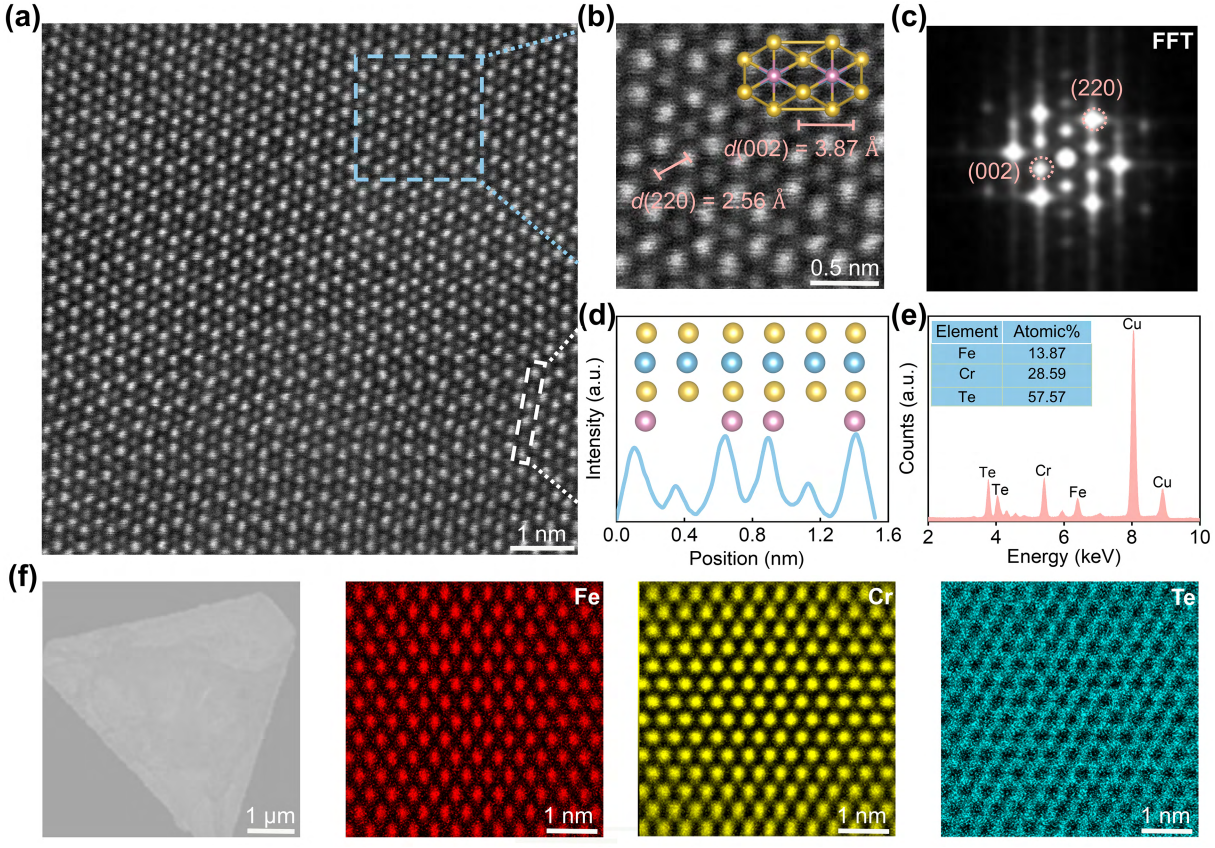

Figure 2 Atomic structural characterization of $FeCr_2Te_4$ nanosheets. (a) Atomic-resolution ADF-STEM image of the samples. (b) Enlarged ADF-STEM image from the blue-boxed region in (a), which is consistent with the atomic arrangement along the [001] zone axis. (c) Corresponding FFT pattern of the region in (a). (d) Intensity line profile of the white rectangular region marked in (a). (e) TEM-EDS spectra. (f) Low-magnification STEM image and corresponding EDS mapping images of Fe, Cr, and Te elements.

line profile extracted from the white-marked region in Fig. 2(a), clearly distinguishing the contrast between bright and dim regions in the ADF-STEM image. These intensity differences originate from the multilayer stacked configurations of Fe, Cr, and Te atoms in the bright regions, whereas the dim regions correspond to areas with fewer stacked Fe atomic layers. Transmission electron microscopy-EDS (TEM-EDS) analysis reveals that Fe, Cr, and Te elements are uniformly distributed within the $FeCr_2Te_4$ nanosheets, with an atomic ratio of approximately 1:1.98:4.01 (Figs. 2(e) and 2(f)). Furthermore, XRD and SEM-EDS characterizations confirm the high crystallinity of the as-synthesized $FeCr_2Te_4$ nanosheets (Figs. S8 and S9 in the ESM).

Subsequently, the magnetic properties of the $FeCr_2Te_4$ nanosheets were investigated using a superconducting quantum interference device (SQUID) and MOKE measurements. The as-grown samples randomly distributed on mica substrates were measured under field-cooled (FC) and zero-field-cooled (ZFC) conditions via SQUID. As shown in Fig. 3(a), *M*–*T* curves were measured under an external magnetic field of 500 Oe. A magnetic phase transition at ~ 122 K was extracted using the first-derivative method, consistent with the reported T_C of bulk samples (Fig. S10(a) in the ESM) [32, 33]. Moreover, the corresponding *M*–*H* curves in Fig. S10(b) in the ESM reveal the magnetic anisotropy of the 2D $FeCr_2Te_4$ nanosheets. To gain deeper insights into the thickness-dependent magnetic properties, MOKE measurements were performed. Figure 3(b) displays the MOKE signals of a 12.4 nm-thick $FeCr_2Te_4$ nanosheet in the temperature range of 5–150 K (Fig. S11(a) in the ESM). As the temperature increases, both the Kerr rotation angle (θ_K) and coercivity (H_C) gradually decrease, eventually forming overlapping loops at 130 K. This transition marks the transformation from the FIM phase to the paramagnetic (PM) phase, where the transition temperature is defined as T_C. Temperature-dependent hysteresis loops of $FeCr_2Te_4$ nanosheets with varying thicknesses were also measured, revealing a consistent T_C of approximately 130 K across different thicknesses (Figs. S12 and S13 in the ESM). Importantly, the T_C of these nanosheets is higher than that of previously reported 2D magnetic materials, such as $Cr_2Ge_2Te_6$ (68 K) [13], $CrSiTe_3$ (33 K) [39]. Notably, an AFM state was observed in the MOKE signal of a 60.2 nm-thick $FeCr_2Te_4$ nanosheet (Fig. 3(c) and Fig. S11(b) in the ESM). At temperatures below 50 K, a standard hysteresis loop was observed, consistent with the formation of a FIM ordered state. Figure 3(d) presents the MOKE signal of the 60.2 nm-thick $FeCr_2Te_4$ nanosheet measured at 5 K, where a clear hysteresis

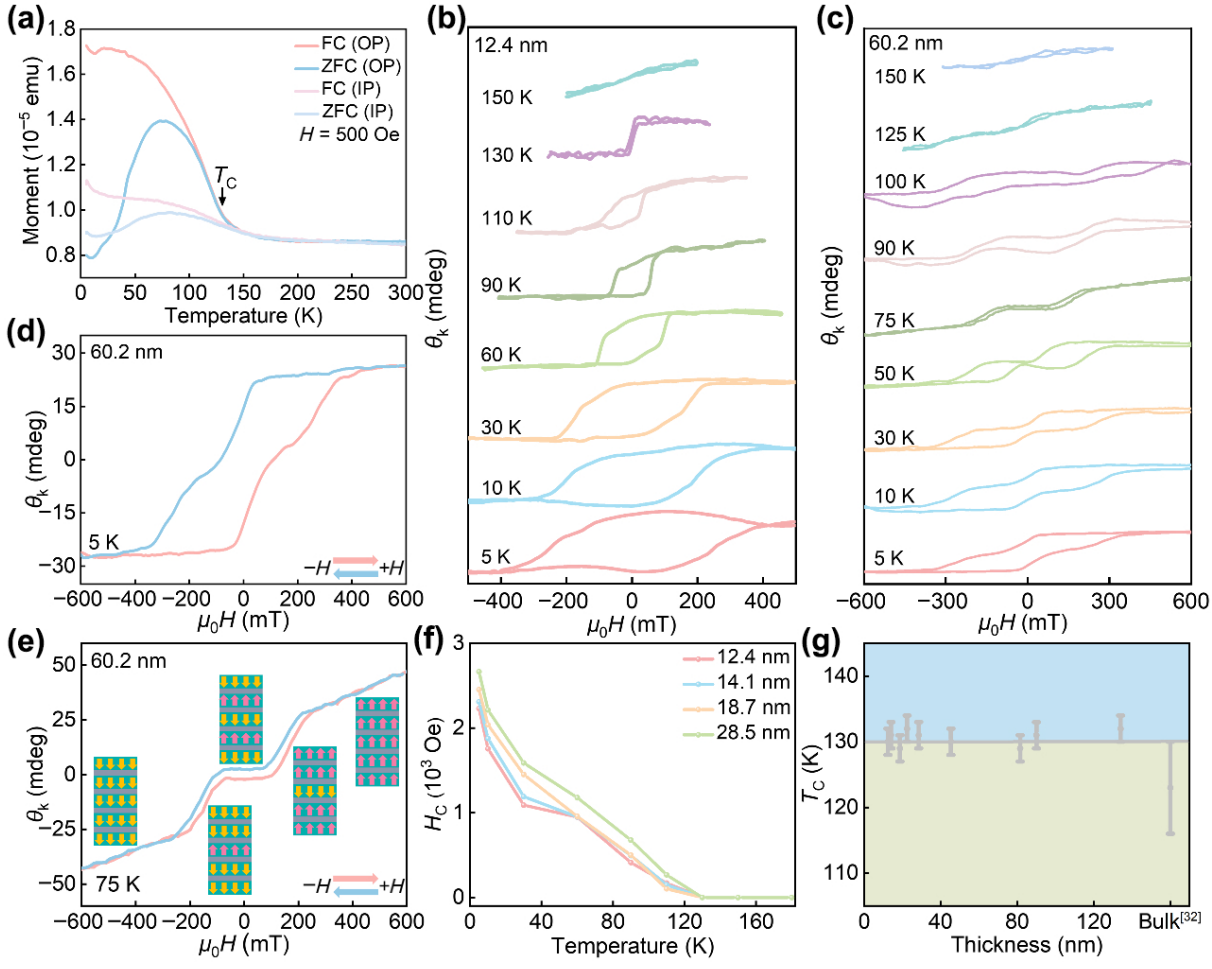

Figure 3 Magnetic properties of $FeCr_2Te_4$ nanosheets. (a) Temperature-dependent magnetization curves of the nanosheets measured under perpendicular and parallel magnetic fields of 500 Oe, respectively. (b) and (c) Polar MOKE signals of 12.4 nm-thick and 60.2 nm-thick nanosheets in the temperature range of 5–150 K. (d) and (e) Polar MOKE signals of a 60.2 nm-thick nanosheet at 5 and 75 K; the inset schematic diagram shows the magnetic states of the nanosheet under an external magnetic field, where pink and yellow arrows represent spin-up and spin-down states, respectively. (f) Temperature-dependent H_C of the nanosheets with different thicknesses. (g) Magnetic phase diagram extracted from MOKE measurements for thickness-dependent T_C of the nanosheets.

loop—a key signature of FM ordering—was observed. In contrast, in the temperature range of 50–75 K, the hysteresis loop exhibited multiple magnetic states. As illustrated in Fig. 3(e), $FeCr_2Te_4$ exhibits five distinct collinear magnetic configurations, undergoing four magnetic ordering transitions: from "↓↓↓↓↓" → "↓↓↑↓↓" → "↓↑↓↑↓" → "↑↑↓↑↑" → "↑↑↑↑↑", where arrows "↑" and "↓" denote spin-up and spin-down states, respectively. At 75 K, the MOKE signal is strongly suppressed within a magnetic field range of approximately ±735 Oe, with θ_K approaching zero. Beyond these critical fields, θ_K gradually recovers to finite values. This behavior is consistent with emerging A-type AFM interlayer coupling [40]. However, the non-zero net magnetization observed at 75 K indicates that the sample is not a strictly collinear AFM, which is likely influenced by the parent compound $CrTe_2$ [41]. We have also systematically investigated the critical thickness range and the reproducibility of the AFM state. Our results indicate that samples with thicknesses of approximately 43.4 and 54.7 nm exhibit purely FIM behavior, with no signature of an AFM state observed. Based on these observations, we infer that the critical thickness for the emergence of the AFM state lies approximately between 54.7 and 60.2 nm. Moreover, stable AFM characteristics analogous to those of the 60.2 nm-thick nanosheet were also observed in nanosheets with thicknesses of 68.6 and 71.4 nm, confirming the excellent reproducibility of this AFM state across multiple nanosheets (Fig. S14 in the ESM).

Next, the underlying mechanisms governing the magnetic behaviors were explored in detail. The FIM ordering in $FeCr_2Te_4$ arises from the competition between two exchange interactions: FM exchange coupling within Cr^{3+}–Te^{2-}–Cr^{3+} bonds and AFM interaction between Cr^{3+}–Fe^{2+} pairs (Fig. S15 in the ESM). Previous theoretical calculations on bulk $FeCr_2Te_4$ with five distinct magnetic configurations have confirmed that the FIM phase possesses the lowest formation energy [32]. The mechanism underlying the emergence of the AFM state in 2D $FeCr_2Te_4$ remains an open question. AFM materials are highly sensitive to variations in lattice constants, especially in structures such as the tilted Cr-Fe-Cr trimer [32]. $FeCr_2Te_4$ adopts a 2R-stacked structure, where Fe atoms are intercalated within the 1T-phase $CrTe_2$ framework. This intercalation reduces the interlayer spacing along the *c*-axis from 6.10 to 5.75 Å [41]. Therefore, we propose that the AFM state may originate from interlayer exchange coupling induced by variations in the vdW interlayer spacing, which further enables a reversible transition between FIM and AFM states upon temperature tuning. Previous studies have demonstrated that the magnetic properties of materials such as $CrSiTe_3$ [42] and Fe_3GeTe_2 [43] can be tuned by adjusting interatomic spacing under moderate strain. Pressure has been shown to reduce the interlayer vdW spacing and modify the stacking order in atomically thin CrI_3, irreversibly driving an interlayer AFM-to-FM phase transition [8]. Additionally, FM-to-AFM transitions have been observed in Cr_5Te_8 [44] and Co-doped Fe_4GeTe_2 [45]. Such modulation of magnetic order originates from changes in the Ruderman–Kittel–Kasuya–Yoshida (RKKY) exchange interaction. In Cr_5Te_8 and Co-doped Fe_4GeTe_2, slight variations in the *c*-axis lattice constant enable the tuning of the RKKY interaction via temperature and doping. Notably, interlayer AFM coupling has been observed in bulk Cr_5Te_8 (150–180 K) and in 12 nm-thick Cr_5Te_8 nanosheets (160–180 K) [22, 44], which is similar to our observation of AFM behavior in $FeCr_2Te_4$ within the 50–75 K range. Thus, the reduced interlayer spacing in 2D $FeCr_2Te_4$ may enhance interlayer coupling, modulates both the magnitude and sign of the RKKY interaction, and facilitates the coexistence of FIM and AFM phases within the 50–75 K window. Specifically, interlayer coupling stabilizes the AFM state in thick nanosheets at specific temperatures, whereas thinner nanosheets retain a stable FIM state due to enhanced interatomic exchange interactions and surface termination effects [28].

To gain further insight into the magnetic properties of $FeCr_2Te_4$ nanosheets, we systematically investigated the temperature and thickness dependence of the H_C and T_C—key parameters of fundamental interest in condensed matter physics. As shown in Fig. 3(f), the H_C values of nanosheets with different thicknesses decrease monotonically with increasing temperatures. Moreover, at a given temperature, H_C decreases as the thickness is reduced. This behavior aligns with observations in other FM materials, such as Fe_3GeTe_2 [11] and Cr_5Te_8 [38]. The T_C values extracted from the MOKE curves of nanosheets with varying thicknesses (Fig. 3(g)) remain constant at approximately 130 K, independent of thickness, and are slightly higher than that of the bulk phase [34]. A similar thickness-independent T_C has been reported in nonlayered metastable Cr_3Te_4 phases, where T_C shows no significant variation even at the 2D limit [46]. This phenomenon is likely attributed to surface atomic terminations.

The transport properties of the samples were characterized using a PPMS. Figure 4(b) presents the OP magnetoresistance (MR) curves of $FeCr_2Te_4$ measured at different temperatures, with the corresponding OM image and thickness of the device shown in Fig. S16 in the ESM. Notably, at all measured temperatures, the MR is enhanced under low magnetic fields but suppressed under high magnetic fields, exhibiting typical negative MR behavior. The low-field MR enhancement originates from the combined effects of the Lorentz force and magnetization rotation, whereas the high-field MR reduction arises from the suppression of spin disorder and spin-dependent carrier scattering [47]. To elucidate the underlying mechanism of the AHE in 2D $FeCr_2Te_4$, we measured the AHE curves of a 45.5 nm-thick $FeCr_2Te_4$ nanosheet at various temperatures (Fig. 4(a)). The AHE is generally attributed to three primary mechanisms: the intrinsic Karplus–Luttinger (KL), skew-scattering, and side-jump scattering. For all temperatures below 130 K, the Hall resistivity curves exhibit a sharp jump at low fields and become linear at high fields, confirming the presence of AHE in the $FeCr_2Te_4$ nanosheets.

For ferromagnetic materials, the Hall resistivity can be expressed as the sum of the ordinary and anomalous contributions [48, 49]

$$\rho_{xy} = \rho^0_{xy} + \rho^A_{xy} = R_0\mu_0 H + R_s M \quad (1)$$

where ρ^0_{xy} and ρ^A_{xy} are the ordinary and anomalous Hall resistivity, respectively; R_0 and R_S are the corresponding Hall coefficients; H is the applied magnetic field; and M is the magnetization. By linearly fitting the high-field region of the ρ_{xy} versus $\mu_0 H$ curve, both the slope (R_0) and the intercept (ρ^A_{xy}) can be obtained. The ordinary Hall coefficient is given by $R_0 = 1/(nq)$, where n is the carrier concentration and q is the electronic charge. Additionally, R_s can be determined from the relation $\rho^A_{xy} = R_s M_s$, where M_s is the saturation magnetization extracted from linear fitting of the high-field M versus $\mu_0 H$ curves. The electrical conductivity is described by [50]

$$\sigma_{xx} = 1/\rho = ne\mu \quad (2)$$

where ρ is the resistivity, e is the charge quantity, and μ is the carrier mobility. The extracted n and μ are shown in Fig. 4(c). The n is

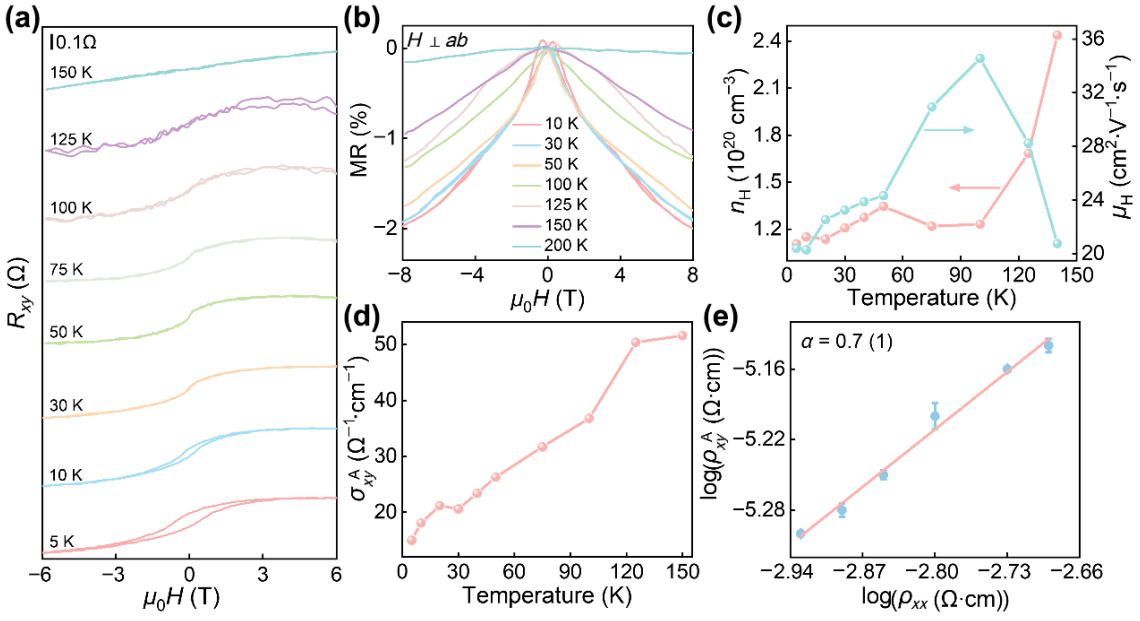

Figure 4 Transport measurements of a 45.5 nm-thick $FeCr_2Te_4$ Hall device. (a) OP R_{xy} hysteresis loops of $FeCr_2Te_4$ measured at different temperatures. (b) MR–H curves of $FeCr_2Te_4$ measured at varied temperatures. (c) and (d) Temperature dependence of carrier density, carrier mobility, and anomalous Hall conductivity. (e) Scaling behavior of anomalous Hall resistivity.

~ 10^{21} cm^{-3}, while the μ peaks at a value of ~ 30 cm^2·V^{-1}·s^{-1}—slightly lower than that of Fe_3GaTe_2 [3] but higher than that of Fe_3GeTe_2 [51]. The anomalous Hall conductivity σ^A_{xy} is calculated as

$$\sigma^A_{xy} = \rho^A_{xy}/(\rho^2_{xx} + \rho^2_{xy}) \quad (3)$$

Figure 4(d) shows the temperature-dependence of σ^A_{xy}. Theoretically, the intrinsic contribution to the anomalous Hall conductivity $\sigma^A_{xy,in}$ is approximately $e^2/(hd)$, where e is the electronic charge, h is the Planck constant, and d is the lattice parameter [52]. For $d \approx 4.3$ Å, $\sigma^A_{xy,in}$ is estimated to be ~ 900 Ω^{-1}·cm^{-1}—far larger than the experimentally observed value in Fig. 4(d), thereby ruling out the intrinsic KL mechanism. The extrinsic side-jump mechanism follows the scaling relation $\rho^A_{xy} = \beta\rho^2_{xx}$. To identify the dominant AHE mechanism, we fitted the ρ^A_{xy} versus ρ_{xx} relationship using the general scaling form $\rho^A_{xy} = \beta\rho^\alpha_{xx}$ (Fig. 4(e)), yielding α ~ 0.7(1). We further investigated the AHE mechanism in 74.5 nm-thick $FeCr_2Te_4$ nanosheets. The experimentally measured anomalous Hall conductivity is lower than the theoretically calculated intrinsic value. Fitting according to the scaling relation $\rho^A_{xy} = \beta\rho^2_{xx}$ yields α ~ 0.8(1) (Fig. S17 in the ESM). Since both the side-jump and intrinsic KL mechanisms exhibit α ~ 2, skew-scattering is likely the dominant mechanism contributing to the AHE in $FeCr_2Te_4$. This mechanism arises from asymmetric scattering of charge carriers by impurities or defects, giving rise to the anomalous Hall effect.

Furthermore, comparative studies of as-grown $FeCr_2Te_4$ nanosheets with those prepared under different conditions reveal that the 2D $FeCr_2Te_4$ nanosheets exhibit excellent stability and corrosion resistance (Fig. S18 in the ESM). Such robustness provides a solid foundation for their application under diverse experimental conditions.

4 Conclusion

In summary, we report the first synthesis of high-quality, submillimeter-scale 2D nonlayered FIM $FeCr_2Te_4$ nanosheets via a dual-confined CVD strategy. The as-grown nanosheets exhibit robust stability under both high-temperature and harsh chemical conditions. The T_C of the samples is independent of thickness. The observed FIM ordering arises from the competition between two exchange interactions: FM exchange coupling within Cr^{3+}–Te^{2-}–Cr^{3+} bonds and AFM interaction between Cr^{3+}–Fe^{2+} pairs. Interestingly, a distinct AFM state emerges in thicker nanosheets within the temperature range of 50–75 K. This AFM state is likely attributed to interlayer exchange coupling induced by variations in vdW interlayer spacing, while the reversible transition between FIM and AFM states can be achieved by tuning the temperature. Furthermore, the nanosheets exhibit an AHE, with n ~ 10^{21} cm^{-3} and μ ~ 30 cm^2·V^{-1}·s^{-1}. Detailed analysis indicates that the AHE is predominantly governed by an extrinsic skew-scattering mechanism. Our work provides crucial insights into the growth of ternary nonlayered tellurides, expands the family of 2D AB_2Te_4 magnetic materials, and advances the fundamental understanding of magnetism in 2D nonlayered systems. Importantly, the excellent stability and tunable magnetic states of 2D $FeCr_2Te_4$ highlight its great potential for applications in compact, ultra-low-power spintronic devices.

Electronic Supplementary Material: Supplementary material (typical EDS mapping images, atomic force microscopy and OM images under different experimental conditions, experimental and simulated ADF-STEM images, XRD patterns, Raman spectra, SEM images, M–T curves, M–H curves, exchange coupling pathways, MOKE curves) is available in the online version of this article at https://doi.org/10.26599/NR.2026.94908675.

Data availability

All data needed to support the conclusions in the paper are presented in the manuscript and the Electronic Supplementary Material. Additional data related to this paper may be requested from the corresponding author upon request.

Acknowledgements

This work was supported by the National Key Research and Development Program of China (No. 2024YFA1410200), the National Natural Science Foundation of China (Nos. U24A6002, 12241403, 52371245, 52501250, and 12274276), the Shanxi Province Basic Research Program (No. 202303021224009), and the Shanxi Province Higher Educational Institutions Young Academic Leaders Program (No. 2024Q015).

Declaration of competing interest

All the contributing authors report no conflict of interests in this work.

Author contribution statement

Z. T. Z., W. Z., and Q. T. J.: Date curation, formal analysis, investigation methodology, validation, writing – original draft. R. K. J. and Y. H.: Methodology, investigation, validation. Z. Z.: Investigation. C. Z.: Resources. H. S. Z.: Theoretical calculations. W. J. C.: Project administration, resources, supervision. W. H. X. and X. H. X.: Conceptualization, funding acquisition, project administration, resources, supervision, writing – review & editing. All the authors have approved the final manuscript.

Use of AI statement

None.

References

[1] Lin, X. Y.; Yang, W.; Wang, K. L.; Zhao, W. S. Two-dimensional spintronics for low-power electronics. *Nat. Electron.* **2019**, *2*, 274–283.

[2] Yang, H.; Valenzuela, S. O.; Chshiev, M.; Couet, S.; Dieny, B.; Dlubak, B.; Fert, A.; Garello, K.; Jamet, M.; Jeong, D. E. et al. Two-dimensional materials prospects for non-volatile spintronic memories. *Nature* **2022**, *606*, 663–673.

[3] Zhang, G. J.; Guo, F.; Wu, H.; Wen, X. K.; Yang, L.; Jin, W.; Zhang, W. F.; Chang, H. X. Above-room-temperature strong intrinsic ferromagnetism in 2D van der Waals Fe_3GaTe_2 with large perpendicular magnetic anisotropy. *Nat. Commun.* **2022**, *13*, 5067.

[4] Bonilla, M.; Kolekar, S.; Ma, Y. J.; Diaz, H. C.; Kalappattil, V.; Das, R.; Eggers, T.; Gutierrez, H. R.; Phan, M. H.; Batzill, M. Strong room-temperature ferromagnetism in VSe_2 monolayers on van der Waals substrates. *Nat. Nanotechnol.* **2018**, *13*, 289–293.

[5] Deng, Y. J.; Yu, Y. J.; Song, Y. C.; Zhang, J. Z.; Wang, N. Z.; Sun, Z. Y.; Yi, Y. F.; Wu, Y. Z.; Wu, S. W.; Zhu, J. Y. et al. Gate-tunable room-temperature ferromagnetism in two-dimensional Fe_3GeTe_2. *Nature* **2018**, *563*, 94–99.

[6] Huang, B.; McGuire, M. A.; May, A. F.; Xiao, D.; Jarillo-Herrero, P.; Xu, X. D. Emergent phenomena and proximity effects in two-dimensional magnets and heterostructures. *Nat. Mater.* **2020**, *19*, 1276–1289.

[7] Silinskas, M.; Senz, S.; Gargiani, P.; Ruiz, A. M.; Kalkofen, B.; Kostanovski, I.; Mohseni, K.; Baldoví, J. J.; Meyerheim, H. L.; Parkin, S. S. P. et al. Self-intercalation as origin of high-temperature ferromagnetism in epitaxially grown Fe_5GeTe_2 thin films. *Phys. Rev. Lett.* **2024**, *133*, 256702.

[8] Li, T. X.; Jiang, S. W.; Sivadas, N.; Wang, Z. F.; Xu, Y.; Weber, D.; Goldberger, J. E.; Watanabe, K.; Taniguchi, T.; Fennie, C. J. et al. Pressure-controlled interlayer magnetism in atomically thin CrI_3. *Nat. Mater.* **2019**, *18*, 1303–1308.

[9] Mounet, N.; Gibertini, M.; Schwaller, P.; Campi, D.; Merkys, A.; Marrazzo, A.; Sohier, T.; Castelli, I. E.; Cepellotti, A.; Pizzi, G. et al. Two-dimensional materials from high-throughput computational exfoliation of experimentally known compounds. *Nat. Nanotechnol.* **2018**, *13*, 246–252.

[10] Wu, S. X.; He, Z. H.; Gu, M. H.; Ren, L. Z.; Li, J. B.; Deng, B.; Wang, D.; Guo, X. H.; Li, W. J.; Chen, M. Y. et al. Robust ferromagnetism in wafer-scale Fe_3GaTe_2 above room-temperature. *Nat. Commun.* **2024**, *15*, 10765.

[11] Jiang, H. N.; Zang, Z. H.; Wang, X. G.; Que, H. F.; Wang, L.; Si, K. P.; Zhang, P.; Ye, Y.; Gong, Y. J. Thickness-tunable growth of composition-controllable two-dimensional Fe_xGeTe_2. *Nano Lett.* **2022**, *22*, 9477–9484.

[12] Zhao, B.; Pandey, L.; Ali, K.; Wang, E. D.; Polley, C. M.; Thiagarajan, B.; Makk, P.; Guimarães, M. H. D.; Dash, S. P. Field-free spin-orbit torque switching of canted van der Waals magnets. *ACS Nano* **2025**, *19*, 13817–13824.

[13] Gong, C.; Li, L.; Li, Z. L.; Ji, H. W.; Stern, A.; Xia, Y.; Cao, T.; Bao, W.; Wang, C. Z.; Wang, Y. et al. Discovery of intrinsic ferromagnetism in two-dimensional van der Waals crystals. *Nature* **2017**, *546*, 265–269.

[14] Huang, B.; Clark, G.; Navarro-Moratalla, E.; Klein, D. R.; Cheng, R.; Seyler, K. L.; Zhong, D.; Schmidgall, E.; McGuire, M. A.; Cobden, D. H. et al. Layer-dependent ferromagnetism in a van der Waals crystal down to the monolayer limit. *Nature* **2017**, *546*, 270–273.

[15] Takagi, R.; Hirakida, R.; Settai, Y.; Oiwa, R.; Takagi, H.; Kitaori, A.; Yamauchi, K.; Inoue, H.; Yamaura, J. I.; Nishio-Hamane, D. et al. Spontaneous Hall effect induced by collinear antiferromagnetic order at room temperature. *Nat. Mater.* **2025**, *24*, 63–68.

[16] Huan, Y. H.; Luo, T. T.; Han, X. C.; Ge, J.; Cui, F. F.; Zhu, L. J.; Hu, J. Y.; Zheng, F. P.; Zhao, X. X.; Wang, L. L. et al. Composition-controllable syntheses and property modulations from 2D ferromagnetic Fe_5Se_8 to metallic Fe_3Se_4 nanosheets. *Adv. Mater.* **2023**, *35*, 2207276.

[17] Zhao, Z. J.; Zhou, J.; Liu, L. H.; Liu, N. S.; Huang, J. Q.; Zhang, B.; Li, W.; Zeng, Y.; Zhang, T.; Ji, W. et al. Two-dimensional room-temperature magnetic nonstoichiometric Fe_7Se_8 nanocrystals: Controllable synthesis and magnetic behavior. *Nano Lett.* **2022**, *22*, 1242–1250.

[18] Kang, L. X.; Ye, C.; Zhao, X. X.; Zhou, X. Y.; Hu, J. X.; Li, Q.; Liu, D.; Das, C. M.; Yang, J. F.; Hu, D. Y. et al. Phase-controllable growth of ultrathin 2D magnetic FeTe crystals. *Nat. Commun.* **2020**, *11*, 3729.

[19] Cheng, M.; Zhao, X. X.; Zeng, Y.; Wang, P.; Wang, Y. Z.; Wang, T.; Pennycook, S. J.; He, J.; Shi, J. P. Phase-tunable synthesis and etching-free transfer of two-dimensional magnetic FeTe. *ACS Nano* **2021**, *15*, 19089–19097.

[20] Cui, F. F.; Zhao, X. X.; Xu, J. J.; Tang, B.; Shang, Q. Y.; Shi, J. P.; Huan, Y. H.; Liao, J. H.; Chen, Q.; Hou, Y. L. et al. Controlled growth and thickness‐dependent conduction-type transition of 2D ferrimagnetic Cr_2S_3 semiconductors. *Adv. Mater.* **2020**, *32*, 1905896.

[21] Jang, J.; Srivastava, P. K.; Joe, M.; Jung, S. G.; Park, T.; Kim, Y.; Lee, C. Half-metallic antiferromagnetic 2D nonlayered Cr_2Se_3 nanosheets. *ACS Nano* **2025**, *19*, 999–1006.

[22] Fu, L.; Llacsahuanga Allcca, A. E.; Chen, Y. P. Coexisting ferromagnetic-antiferromagnetic state and giant anomalous hall effect in chemical vapor deposition-grown 2D Cr_5Te_8. *ACS Nano* **2024**, *18*, 33381–33389.

[23] Jiang, Q. T.; Yang, H. L.; Xue, W. H.; Yang, R. L.; Shen, J. L.; Zhang, X. Y.; Li, R. W.; Xu, X. H. Controlled growth of submillimeter-scale Cr_5Te_8 nanosheets and the domain wall nucleation governed magnetization reversal process. *Nano Lett.* **2024**, *24*, 1246–1253.

[24] Wang, H.; Wen, Y.; Zhao, X. X.; Cheng, R. Q.; Yin, L.; Zhai, B. X.; Jiang, J.; Li, Z. W.; Liu, C. S.; Wu, F. C. et al. Heteroepitaxy of 2D $CuCr_2Te_4$ with robust room-temperature ferromagnetism. *Adv. Mater.* **2023**, *35*, 2211388.

[25] Yang, S.; Li, Z. L.; Lin, C. J.; Yi, C. J.; Shi, Y. G.; Culcer, D.; Li, Y. Q. Unconventional temperature dependence of the anomalous Hall effect in $HgCr_2Se_4$. *Phys. Rev. Lett.* **2019**, *123*, 096601.
[26] Hemberger, J.; Rudolf, T.; Krug von Nidda, H. A.; Mayr, F.; Pimenov, A.; Tsurkan, V.; Loidl, A. Spin-driven phonon splitting in bond-frustrated $ZnCr_2S_4$. *Phys. Rev. Lett.* **2006**, *97*, 087204.
[27] Yang, H.; Wang, F.; Zhang, H. S.; Guo, L. H.; Hu, L. Y.; Wang, L. F.; Xue, D. J.; Xu, X. H. Solution synthesis of layered van der Waals (vdW) ferromagnetic $CrGeTe_3$ nanosheets from a non-vdW Cr_2Te_3 template. *J. Am. Chem. Soc.* **2020**, *142*, 4438–4444.
[28] Liu, L.; Yu, Q.; Xia, J.; Shi, W. X.; Wang, D.; Wu, J. X.; Xie, L. M.; Chen, Y. S.; Jiao, L. Y. 2D Air-stable nonlayered ferrimagnetic $FeCr_2S_4$ crystals synthesized via chemical vapor deposition. *Adv. Mater.* **2024**, *36*, 2401338.
[29] Liu, L.; Yu, Q.; Wu, J. X.; Xia, J.; Wang, D.; Xie, L. M.; Chen, Y. S.; Jiao, L. Y. Atmospheric pressure synthesis of ultrathin monoclinic $FeCr_2S_4$ crystals with robust antiferromagnetism. *J. Am. Chem. Soc.* **2025**, *147*, 19614–19621.
[30] Snyder, G. J.; Caillat, T.; Fleurial, J. P. Thermoelectric, transport, and magnetic properties of the polaron semiconductor $Fe_xCr_{3-x}Se_4$. *Phys. Rev. B* **2000**, *62*, 10185.
[31] Ok, H. N.; Lee, C. S. Mössbauer study of monoclinic $FeCr_2Se_xS_{4-x}$. *Phys. Rev. B* **1986**, *33*, 581–584.
[32] Liu, Y.; Koch, R. J.; Hu, Z. X.; Aryal, N.; Stavitski, E.; Tong, X.; Attenkofer, K.; Bozin, E. S.; Yin, W. G.; Petrovic, C. Three-dimensional Ising ferrimagnetism of Cr–Fe–Cr trimers in $FeCr_2Te_4$. *Phys. Rev. B* **2020**, *102*, 085158.
[33] Liu, Y.; Tan, H. X.; Hu, Z. X.; Yan, B. H.; Petrovic, C. Anomalous Hall effect in the weak-itinerant ferrimagnet $FeCr_2Te_4$. *Phys. Rev. B* **2021**, *103*, 045106.
[34] Routh, S.; Kar, I.; Low, A.; Ghosh, S.; Bhowmik, T. K. Magnetoresistance behavior across the critical region in ferrimagnet $FeCr_2Te_4$ single crystal. *Phys. Lett. A* **2023**, *486*, 129101.
[35] Wen, Y.; Liu, Z. H.; Zhang, Y.; Xia, C. X.; Zhai, B. X.; Zhang, X. H.; Zhai, G. H.; Shen, C.; He, P.; Cheng, R. Q. et al. Tunable room-temperature ferromagnetism in two-dimensional Cr_2Te_3. *Nano Lett.* **2020**, *20*, 3130–3139.
[36] Zhou, S. S.; Gan, L.; Wang, D. L.; Li, H. Q.; Zhai, T. Y. Space-confined vapor deposition synthesis of two dimensional materials. *Nano Res.* **2018**, *11*, 2909–2931.
[37] Zhou, J. D.; Lin, J. H.; Huang, X. W.; Zhou, Y.; Chen, Y.; Xia, J.; Wang, H.; Xie, Y.; Yu, H. M.; Lei, J. C. et al. A library of atomically thin metal chalcogenides. *Nature* **2018**, *556*, 355–359.
[38] Tang, B. J.; Wang, X. W.; Han, M. J.; Xu, X. D.; Zhang, Z. W.; Zhu, C.; Cao, X.; Yang, Y. M.; Fu, Q. D.; Yang, J. Q. et al. Phase engineering of Cr_5Te_8 with colossal anomalous Hall effect. *Nat. Electron.* **2022**, *5*, 224–232.
[39] Williams, T. J.; Aczel, A. A.; Lumsden, M. D.; Nagler, S. E.; Stone, M. B.; Yan, J. Q.; Mandrus, D. Magnetic correlations in the quasi-two-dimensional semiconducting ferromagnet $CrSiTe_3$. *Phys. Rev. B* **2015**, *92*, 144404.
[40] Cheng, G. H.; Rahman, M. M.; Allcca, A. L.; Rustagi, A.; Liu, X. T.; Liu, L. N.; Fu, L.; Zhu, Y. L.; Mao, Z. Q.; Watanabe, K. et al. Electrically tunable moiré magnetism in twisted double bilayers of chromium triiodide. *Nat. Electron.* **2023**, *6*, 434–442.
[41] Meng, L. J.; Zhou, Z.; Xu, M. Q.; Yang, S. Q.; Si, K. P.; Liu, L. X.; Wang, X. G.; Jiang, H. N.; Li, B. X.; Qin, P. X. et al. Anomalous thickness dependence of Curie temperature in air-stable two-dimensional ferromagnetic 1T-$CrTe_2$ grown by chemical vapor deposition. *Nat. Commun.* **2021**, *12*, 809.
[42] Zhang, C.; Gu, Y.; Wang, L.; Huang, L. L.; Fu, Y.; Liu, C.; Wang, S. M.; Su, H. M.; Mei, J. W.; Zou, X. L. et al. Pressure-enhanced ferromagnetism in layered $CrSiTe_3$ flakes. *Nano Lett.* **2021**, *21*, 7946–7952.
[43] Wang, Y.; Wang, C.; Liang, S. J.; Ma, Z. C.; Xu, K.; Liu, X. W.; Zhang, L. L.; Admasu, A. S.; Cheong, S. W.; Wang, L. Z. et al. Strain-sensitive magnetization reversal of a van der Waals magnet. *Adv. Mater.* **2020**, *32*, 2004533.
[44] Zhang, X. Q.; Liu, W. Q.; Niu, W.; Lu, Q. S.; Wang, W.; Sarikhani, A.; Wu, X. H.; Zhu, C. H.; Sun, J. B.; Vaninger, M. et al. Self-intercalation tunable interlayer exchange coupling in a synthetic van der Waals antiferromagnet. *Adv. Funct. Mater.* **2022**, *32*, 2202977.
[45] Wang, M. J.; Zhu, K. J.; Lei, B.; Deng, Y. Z.; Hu, T.; Song, D. S.; Du, H. F.; Tian, M. L.; Xiang, Z. J.; Wu, T. et al. Layer-number-dependent magnetism in the co-doped van der Waals ferromagnet Fe_3GaTe_2. *Nano Lett.* **2024**, *24*, 4141–4149.
[46] Wang, Y.; Kajihara, S.; Matsuoka, H.; Saika, B. K.; Yamagami, K.; Takeda, Y.; Wadati, H.; Ishizaka, K.; Iwasa, Y.; Nakano, M. Layer-number-independent two-dimensional ferromagnetism in Cr_3Te_4. *Nano Lett.* **2022**, *22*, 9964–9971.
[47] Wang, H.; Wen, Y.; Zhang, X. L.; Zhai, B. X.; Cheng, R. Q.; Yin, L.; Yu, Y. L.; Li, Y. S.; Jiang, J.; Zhu, H. et al. Revealing enhanced optical nonlinearity and robust ferromagnetism in atomically sharp stacking binary-ternary magnetic heterostructures. *ACS Nano* **2024**, *18*, 22978–22988.
[48] Wang, Q.; Sun, S. S.; Zhang, X.; Pang, F.; Lei, H. C. Anomalous Hall effect in a ferromagnetic Fe_3Sn_2 single crystal with a geometrically frustrated Fe bilayer Kagome lattice. *Phys. Rev. B* **2016**, *94*, 075135.
[49] Onoda, S.; Sugimoto, N.; Nagaosa, N. Quantum transport theory of anomalous electric, thermoelectric, and thermal Hall effects in ferromagnets. *Phys. Rev. B* **2008**, *77*, 165103.
[50] Novoselov, K. S.; Geim, A. K.; Morozov, S. V.; Jiang, D.; Zhang, Y.; Dubonos, S. V.; Grigorieva, I. V.; Firsov, A. A. Electric field effect in atomically thin carbon films. *Science* **2004**, *306*, 666–669.
[51] Liu, S. S.; Yuan, X.; Zou, Y. C.; Sheng, Y.; Huang, C.; Zhang, E. Z.; Ling, J. W.; Liu, Y. W.; Wang, W. Y.; Zhang, C. et al. Wafer-scale two-dimensional ferromagnetic Fe_3GeTe_2 thin films grown by molecular beam epitaxy. *npj 2D Mater. Appl.* **2017**, *1*, 30.
[52] Onoda, S.; Sugimoto, N.; Nagaosa, N. Intrinsic versus extrinsic anomalous Hall effect in ferromagnets. *Phys. Rev. Lett.* **2006**, *97*, 126602.